PHYSICAL REVIEW B **80**, 235127 (2009)

# Simulation of two-dimensional quantum systems using a tree tensor network that exploits the entropic area law

L. Tagliacozzo, G. Evenbly, and G. Vidal
*School of Physical Sciences, The University of Queensland, Queensland 4072, Australia*
(Received 13 September 2009; revised manuscript received 18 November 2009; published 18 December 2009)

This work explores the use of a tree tensor network ansatz to simulate the ground state of a local Hamiltonian on a two-dimensional lattice. By exploiting the entropic area law, the tree tensor network ansatz seems to produce quasiexact results in systems with sizes well beyond the reach of exact diagonalization techniques. We describe an algorithm to approximate the ground state of a local Hamiltonian on a $L \times L$ lattice with the topology of a torus. Accurate results are obtained for $L=\{4,6,8\}$, whereas approximate results are obtained for larger lattices. As an application of the approach, we analyze the scaling of the ground-state entanglement entropy at the quantum critical point of the model. We confirm the presence of a positive additive constant to the area law for half a torus. We also find a logarithmic additive correction to the entropic area law for a square block. The single copy entanglement for half a torus reveals similar corrections to the area law with a further term proportional to $1/L$.

DOI: 10.1103/PhysRevB.80.235127 PACS number(s): 64.60.ae, 64.60.an, 64.60.De, 65.40.gd

## I. INTRODUCTION

The numerical study of many-body quantum systems is a challenging task. The exponential growth of the dimension of the Hilbert space with the size of the system implies that exact diagonalization techniques can only be applied to address small lattice systems.[1–3] Quantum Monte Carlo sampling offers a valuable route to the study of larger lattices, although systems of frustrated quantum spins or interacting fermions cannot be analyzed due to the so called *sign problem*.

In two spatial dimensions, the use of a tensor network ansatz, such as the tensor product state or projected entangled pair state (PEPS) (Refs. 4–11) and the multiscale entanglement renormalization ansatz (MERA),[12–15] has opened a very promising alternative path to investigating ground state properties of arbitrarily large lattice systems. The key of these approaches is the ability of the TPS, PEPS, and MERA to reproduce the scaling of the entanglement in the ground state, as given by the entropic area law.

In this work we explore the use of yet another tensor network variational ansatz, namely, a *tree tensor network* (TTN),[16–23] to simulate the ground state of local two-dimensional (2D) lattice systems. This very simple ansatz is inspired on the original real-space renormalization group ideas of Kadanoff and co-workers.[24–29]

The present approach is both motivated and limited by the area law for the entanglement entropy.[30–35] The "area law" is a conjectured property of the entanglement entropy of certain ground states of local Hamiltonians. It asserts that the entropy of a region of the system is proportional to the size of its boundary rather than proportional to its volume. Direct calculations of the entanglement entropy have provided evidence of the validity of the area law for a large class of systems.[30–33] A complete characterization of the Hamiltonians whose ground state obeys the area law is still missing.

On the one hand, by exploiting the area law a TTN can be used to address small 2D lattices with sizes well beyond the reach of exact diagonalization techniques. Specifically, the cost of simulating a lattice of $L \times L$ sites grows as $\exp(L)$ instead of $\exp(L^2)$. Thus, the TTN approach is useful to investigate small 2D quantum systems and to study larger systems with finite-size scaling techniques. It is also particularly suitable to investigate ground-state entropies.

On the other hand, the $\exp(L)$ cost due to the entropic area law still sets a severe limit to the system sizes a TTN can describe and the present approach simply cannot compete with the PEPS and MERA algorithms[4,6,10,11,14] for large systems. However, the TTN is also of interest in the context of developing these more advanced, scalable algorithms. This is due both to its simplicity and to its direct connection to ground state entanglement properties, on which the scalable algorithms are also based. As a matter of fact, the TTN approach described in this work was initially developed as an auxiliary tool to help in the design of the MERA.[14]

The present approach bears important similarities with White's *density matrix renormalization group* (DMRG) (Refs. 36–38) (for a review see, e.g., Ref. 39) when applied to 2D lattice systems.[40–46] Roughly speaking, it can be regarded as a DMRG approach where the *matrix product state* has been replaced with a TTN. This replacement has both advantages and disadvantages. Its weakest point is an increase in computational cost. However, a TTN greatly improves the connectivity between lattice sites, possibly resulting in faster convergence and better correlation functions (e.g., on a torus). Extracting certain entropies from the TTN, say the entropy of one quarter of the lattice, is straightforward. Finally, the algorithm can be very simply implemented.

The results are organized in several sections. In Sec. II we describe the TTN for 2D lattices and motivate its use in terms of the entropic area law. In Sec. III we explain how to compute the expectation value of local operators, two-point correlation functions, fidelities, and block entropies. Then in Sec. IV we describe an algorithm to approximate ground states with a TTN. This algorithm is tested in Sec. V by addressing the quantum Ising model with transverse magnetic field on a torus made of $L \times L$ sites. Quasiexact results

 

are obtained for lattices of linear size $L=\{4,6,8\}$, whereas approximate results are obtained for $L=\{10,16,32\}$, we also check the exponential cost of a TTN representation and introduce a possible estimate of the error induced by the finite amount of computational resources.

In Sec. VI we turn our attention to the computation of ground-state entanglement at the critical point. We present results for $L=\{4,6,8,10\}$ for both entanglement entropy and single copy entanglement. This allows us to investigate the form of their finite-size scaling. Several authors[47–56] have predicted the presence of corrections to the area law including a universal and positive constant term for half a torus.[50,51,54] Our results reproduce this term, as well as a logarithmic correction for a quarter of a torus.[48,52,55,56] Numerical estimates of the coefficients for all the corrections are presented in Eqs. (41), (42), (45), and (49)–(51). We conclude with a discussion of the results in Sec. VII.

## II. TREE TENSOR NETWORK ANSATZ

In this section we introduce the variational ansatz used throughout the manuscript and justify its applicability in terms of the area law for entanglement entropy.

### A. Isometric tree tensor network

We consider a square lattice $\mathcal{L}$ made of $N=L\times L$ sites, where each site is described by a local Hilbert space $\mathbb{V}$ of finite dimension $d$. Our goal is to represent a pure state $|\Psi\rangle \in \mathbb{V}^{\otimes N}$ of the lattice $\mathcal{L}$. Most of the time, $|\Psi\rangle$ will correspond to the ground state $|\Psi_{\mathrm{GS}}\rangle$ of some local Hamiltonian $H$ defined on $\mathcal{L}$.

A generic state $|\Psi\rangle \in \mathbb{V}^{\otimes N}$ can always be expanded as

$$|\Psi\rangle = \sum_{i_1=1}^{d}\sum_{i_2=1}^{d}\cdots\sum_{i_N=1}^{d} T_{i_1 i_2\cdots i_N}|i_1\rangle|i_2\rangle\cdots|i_N\rangle, \tag{1}$$

where the $d^N$ coefficients $T_{i_1 i_2\cdots i_N}$ are complex numbers and the vectors $\{|1_s\rangle,|2_s\rangle,\ldots,|d_s\rangle\}$ denote a local basis on site $s \in \mathcal{L}$. We refer to the index $i_s$ that labels a local basis for site $s$ $(i_s=1,\ldots,d)$ as a *physical* index.

In this work we further expand the tensor of coefficients $T_{i_1 i_2\cdots i_N}$ in Eq. (1) using a TTN. As shown in Fig. 1 for lattices of $2\times 2$ and $4\times 4$ sites, a TTN decomposition consists of a collection of tensors $w$ that have both *bond* indices and *physical* indices. The tensors are interconnected by the bond indices according to a tree pattern. The $N$ physical indices correspond to the leaves of the tree. Upon summing over all the bond indices, the TTN produces the $d^N$ complex coefficients $T_{i_1 i_2\cdots i_N}$ of Eq. (1).

The tensors in the TTN will be constrained to be *isometric*, in the following sense. As shown in Fig. 2 for the $4\times 4$ case of Fig. 1, each tensor $w$ in a TTN has at most one upper leg/index $\alpha$ and some number $p$ of lower indices/legs $\beta_1,\ldots,\beta_p$, so that its entries read $(w)^{\alpha}_{\beta_1\cdots\beta_p}$. Then we impose that

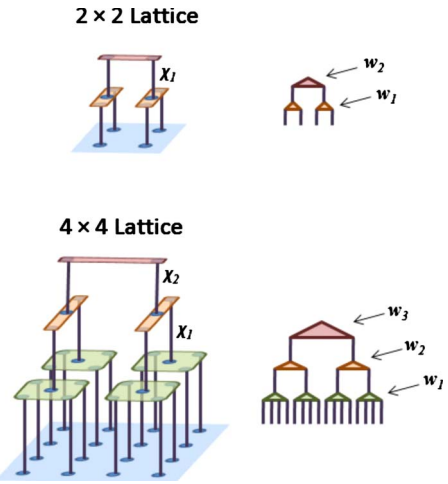


FIG. 1. (Color online) Example of TTN for a $2\times 2$ lattice and a $4\times 4$ lattice. Notice (right) that the TTN for a 2D lattice can always be represented as a planar graph, with the leaves or physical indices ordered on a line. The tensors labeled with $w_i$ are isometric tensors. They act locally by projecting the ground state onto its local support with dimension $\chi_i$ (see Sec. II for further explanation).

$$\sum_{\beta_1\cdots\beta_p}(w)^{\alpha}_{\beta_1\cdots\beta_p}(w^{\dagger})^{\beta_1\cdots\beta_p}_{\alpha'} = \delta_{\alpha\alpha'}. \tag{2}$$

For the sake of clarity, throughout the paper we use diagrams to represent tensor networks as well as tensor manipulations. For instance, the constraints for the tensors $w_1$, $w_2$, and $w_3$ of the TTN of Fig. 1 for a $4\times 4$ lattice, namely,

$$\sum_{\beta_1\beta_2\beta_3\beta_4}(w_1)^{\alpha}_{\beta_1\beta_2\beta_3\beta_4}(w_1^{\dagger})^{\beta_1\beta_2\beta_3\beta_4}_{\alpha'} = \delta_{\alpha\alpha'}, \tag{3}$$

$$\sum_{\beta_1\beta_2}(w_2)^{\alpha}_{\beta_1\beta_2}(w_2^{\dagger})^{\beta_1\beta_2}_{\alpha'} = \delta_{\alpha\alpha'}, \tag{4}$$

$$\sum_{\beta_1\beta_2}(w_3)_{\beta_1\beta_2}(w_3^{\dagger})^{\beta_1\beta_2} = 1, \tag{5}$$

are represented as diagrams in Fig. 2(ii). We refer to a tensor

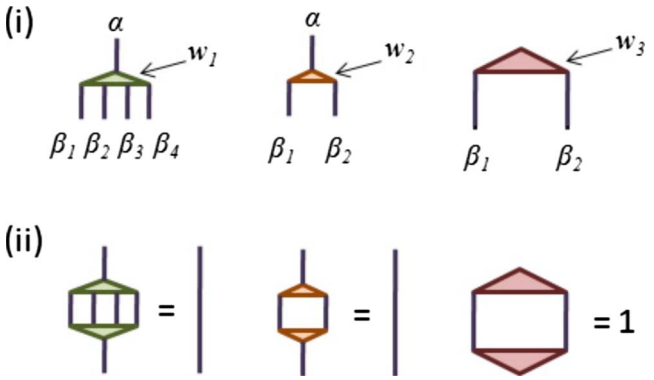


FIG. 2. (Color online) (i) Diagrammatic representation of three types of isometric tensors in the TTN for a $4\times 4$ lattice in Fig. 1. (ii) Graphical representation of the constraints in Eqs. (3)–(5) fulfilled by the isometric tensors.

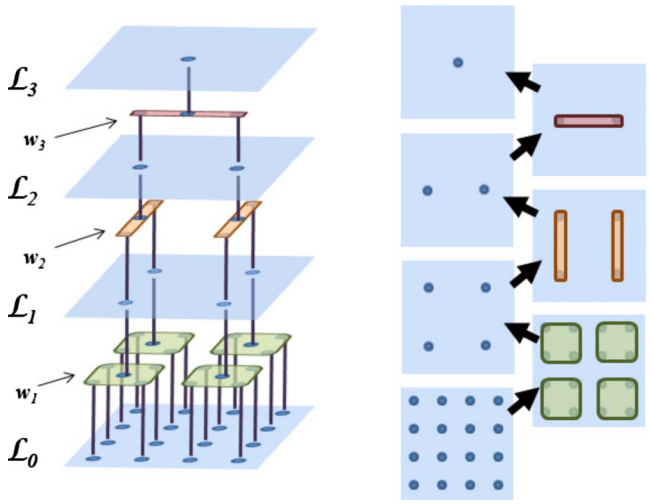


FIG. 3. (Color online) The isometric TTN of Fig. 1 for a $4\times4$ lattice $\mathcal{L}_0$ is associated with a coarse-graining transformation that generates a sequence of increasingly coarse-grained lattices $\mathcal{L}_1$, $\mathcal{L}_2$, and $\mathcal{L}_3$. Notice that in this example we have added an extra index to the top isometry $w_3$, corresponding to the single site of an extra top lattice $\mathcal{L}_3$, which we can use to encode in the TTN a whole subspace of $\mathbb{V}^{\otimes N}$ instead of a single state $|\Psi\rangle$.

$w$ that fulfils Eq. (2) as an *isometry*. As we will see in Secs. III and IV, the use of isometries simplifies the manipulations necessary to compute expectation values of local operators and the spectrum of reduced density matrices, as well as to optimize the TTN. The isometric character of the tensors can also be seen to prevent numerical instability during the simulations.

### B. Coarse graining of the lattice

An intuitive interpretation of the use of a TTN to represent a state $|\Psi\rangle$ can be obtained in terms of a coarse-graining transformation for the lattice $\mathcal{L}$. Notice that the isometries $w$ in Fig. 1 are organized in layers. The bond indices between two layers can be interpreted as defining the sites of an effective lattice. In other words, the TTN defines a sequence of increasingly coarser lattices $\{\mathcal{L}_0,\mathcal{L}_1,\ldots,\mathcal{L}_{T-1}\}$, where $\mathcal{L}_0 \equiv \mathcal{L}$ and each site of lattice $\mathcal{L}_\tau$ is defined in terms of several sites of $\mathcal{L}_{\tau-1}$ by means of an isometry $w_\tau$, see Fig. 3.

In this picture, a site of the lattice $\mathcal{L}_\tau$ effectively corresponds to some number $n_\tau$ of sites of the original lattice $\mathcal{L}_0$. For instance, each of the two sites of $\mathcal{L}_2$ in Fig. 3 corresponds to eight sites of $\mathcal{L}_0$. Similarly, each site of lattice $\mathcal{L}_1$ corresponds to four sites of $\mathcal{L}_0$.

### C. Entropic area law

In using a TTN to represent a generic state $|\Psi\rangle$, the top tensor $w_T$ must already depend on $d^N$ coefficients. It is then unclear that the use of a TTN has any computational advantage with respect to directly dealing with all the $d^N$ coefficients $T_{i_1 i_2 \cdots i_N}$ in Eq. (1). However, ground states $|\Psi_{\mathrm{GS}}\rangle$ of local Hamiltonians are known to often exhibit a so-called entropic *area law*[30–35] and this property might lead to a reduction in computational costs when expressing the state (or an accurate approximation of it) as a TTN.

Let us present the reduced density matrix $\rho$ for a block $A$ of contiguous sites of $\mathcal{L}$ as

$$\rho^A = \mathrm{tr}_B|\Psi\rangle\langle\Psi| = \sum_\alpha p_\alpha |\Psi_\alpha^A\rangle\langle\Psi_\alpha^A|, \tag{6}$$

where $B$ are all the sites of $\mathcal{L}$ outside the block $A$ and $p_\alpha$ are the eigenvalues of $\rho^A$ (that is, $\rho^A|\Psi_\alpha^A\rangle = p_\alpha|\Psi_\alpha^A\rangle$). Then the entropy $S(A)$ of block $A$ is defined as

$$S(A) \equiv -\mathrm{tr}(\rho^A \log \rho^A) = -\sum_\alpha p_\alpha \log p_\alpha. \tag{7}$$

This entropy measures the amount of entanglement between the block $A$ and the rest $B$ of the lattice $\mathcal{L}$, and it is also known as *entanglement entropy*.[57] For a generic state, the entropy of a block $A$ is proportional to the number $n(A)$ of sites in $A$ [provided $n(A) \leq N/2$], that is

$$S(A) \approx n(A)\log d \quad \text{(generic)}. \tag{8}$$

For instance, the entropy of a block made of $l\times l$ sites is proportional to $l^2$ and, correspondingly, the effective dimension $\chi$ required to describe the block (throughout the paper we use a number of different subscripts to denote different effective dimensions $\chi$. For instance, $\chi_{l\times l}$, $\chi(A)$, and $\chi_{1/2}$ refer, respectively, to the effective dimension for a block of $l\times l$ sites, a block $A$ and one half of the lattice. The specific meaning should be clear from the context) is exponential in $l^2$,

$$S_{l\times l} \approx l^2 \log d, \quad \chi_{l\times l} = d^{l^2} \quad \text{(generic)}. \tag{9}$$

If instead the entropy of the block $A$ grows proportional to the number of sites of the boundary of $A$, denoted by $\Sigma(A)$, we say that the state $|\Psi\rangle$ fulfils an entropic "area law"

$$S(A) \approx c_1 \Sigma(A) \quad \text{(area law)}, \tag{10}$$

where $c_1$ is some constant. For instance, for the above block of $l\times l$ sites, the entropy is only proportional to $l$. Accordingly, the dimension $\chi$ required to effectively describe the block may grow markedly less with $l$ than in the generic case,

$$S_{l\times l} \approx 4c_1 l, \quad \chi_{l\times l} \geq \exp(4c_1 l) \quad \text{(area law)}, \tag{11}$$

where the lower bound for $\chi$ is obtained by exponentiating the entropy and is saturated by a flat probability distribution $p_\alpha = 1/\chi$ and $\alpha = 1,\ldots,\chi$.

Equation (11) is our main justification for attempting to describe ground states of local $2D$ Hamiltonians using a TTN. It suggests that it might be possible to accurately approximate a ground state $|\Psi_{\mathrm{GS}}\rangle$ that fulfils the area law of Eq. (10) by using a number of coefficients that scales with the linear size $L$ of the lattice $\mathcal{L}$ only as $O[\exp(L)]$, instead of $O[\exp(L^2)]$ as is the case for a generic state. In other words, ground states of local Hamiltonians are typically less entangled than generic states, and we might be able to exploit this fact computationally.

A simple example of ground state that fulfills the boundary law is a valence bond crystal (as, e.g., it is the ground

TABLE I. Length of the boundaries of different subregions of a 2D lattice system for several choices of topology of the whole system.

| | Plane | Cylinder | Torus |
|---|---|---|---|
| $\Sigma_{1/2}$ | $L$ | $L$ | $2L$ |
| $\Sigma_{1/4}$ | $L$ | $\frac{3}{2}L$ | $2L$ |
| $\Sigma_{1/8}$ | $\frac{5}{4}L$ | $\frac{3}{2}L$ | $\frac{3}{2}L$ |

state of the AKLT model)[58] made of short-range dimers. Each dimer crossing the boundaries of a region $A$ contributes a constant amount to the entropy and the number of such dimers is proportional to the size of the boundary of the region $A$. This roughly corresponds to the presence, in the spectrum of the reduced density matrix, of a number of significant eigenvalues that grows exponentially with the size of the boundary.

### D. Plane, cylinder, and torus

Let us now assume that the entropic boundary law in Eq. (10) translates into an effective site dimension given by

$$\chi(A) \approx \exp[S(A)] \approx \exp[c_1 \sigma(A)], \tag{12}$$

and let us explore the implications that this expression would have on the ability of a TTN to encode ground states.

For this purpose, let us consider the (interacting) boundaries, denoted $\Sigma_{1/2}$, $\Sigma_{1/4}$, and $\Sigma_{1/8}$, of blocks that consists, respectively, of one half, one fourth and one eighth of a $L \times L$ lattice $\mathcal{L}$. These boundaries depend on the topology of the interactions of $H$ on $\mathcal{L}$, and for the plane, cylinder and torus are presented in Table I (see also Fig. 4).

From Table I and Eq. (12) one can obtain the dimension $\chi$ of the sites of the most coarse-grained lattices $\mathcal{L}_{T-1}$, $\mathcal{L}_{T-2}$, and $\mathcal{L}_{T-3}$, and the size of the isometries at the upper layers of the TTN, which is what dominates the computational cost of the approach. The table shows that ground states on a torus

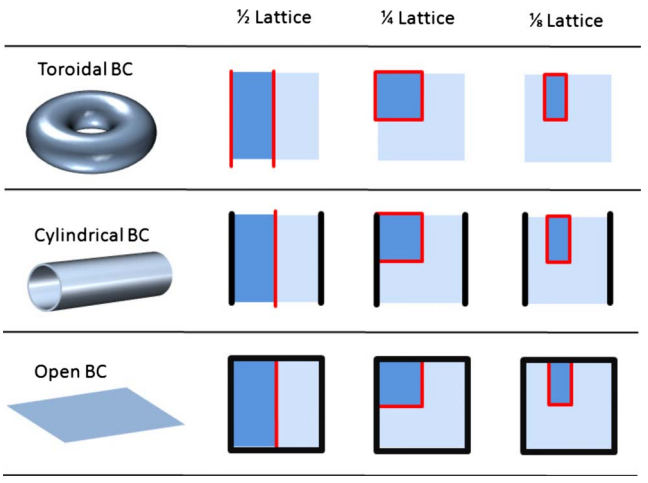


FIG. 4. (Color online) Interacting boundaries $\Sigma_{1/2}$, $\Sigma_{1/4}$, and $\Sigma_{1/8}$ corresponding to one half, one quarter and one eighth of a lattice for three different choices of boundary conditions.

are more entangled (e.g., the blocks have more interacting boundary, or entropy), and therefore computationally more demanding than on a plane or cylinder. In this work we shall concentrate on the torus, with the understanding that a similar analysis can also be conducted for the other cases. (In particular, as it is easy to anticipate, given the same computational costs, larger systems can be addressed in the cases of plane and cylinder interaction topologies.)

### E. TTN ansatz on the torus

From now on we consider a $L \times L$ lattice $\mathcal{L}$ on the torus. In this case, $\chi_{1/2} \approx \chi_{1/4} \approx \exp(c_1 2L)$ are the largest effective site dimensions. The top isometry $w_T$ depends on $\chi_{1/2}^2 \approx \exp(4c_1 L)$ parameters, whereas each isometry $w_{T-1}$ depends on $\chi_{1/2}\chi_{1/4}^2 \approx \exp(6c_1 L)$ parameters. Isometries at lower layers of the TTN can be seen to depend on less parameters.

Based on these observations, our TTN ansatz for the ground state of an $L \times L$ lattice with torus topology and site dimension $d=2$ (e.g., spin-$\frac{1}{2}$ model) will invariably consists of a top isometry $w_T$ and two isometries $w_{T-1}$ with bond dimension $\chi$ on all their indices. Then, depending on the size $L$ and other considerations, the TTN will be completed in two possible ways. For small $L$ ($L \leq 8$ in the examples of Sec. V), a single extra layer of isometries will be considered, where each isometry maps $N/4$ sites of $\mathcal{L}$ directly into one site of $\mathcal{L}_{T-2}$. For larger lattices, it is computationally favorable to complete the TTN with at least two more layers of isometries, see Fig. 5.

Because the isometries $w_{T-1}$ are, by far, the largest tensors in the TTN, the memory required to store the ansatz is a function of the size of $w_{T-1}$, namely,

$$\text{memory} \approx \chi^3 \quad (\text{large } \chi \text{ regime}), \tag{13}$$

where, unless otherwise specified, from now on $\chi$ refers to the effective dimension used for both one half and one quarter of the lattice, $\chi \equiv \chi_{1/2} = \chi_{1/4}$.

### F. Nested Schmidt decompositions

It is instructive to relate the TTN ansatz with the Schmidt decomposition of the state $|\Psi\rangle$ it represents. Recall that given a bipartition $A:B$ of the sites of lattice $\mathcal{L}$ into two subsets $A$ and $B$, the Schmidt decomposition of state $|\Psi\rangle$ according to this bipartition reads

$$|\Psi\rangle = \sum_{\alpha=1}^{\chi(A:B)} \sqrt{p_\alpha} |\Psi_\alpha^A\rangle |\Psi_\alpha^B\rangle, \tag{14}$$

where $p_\alpha$, $|\Psi_\alpha^A\rangle$, and $|\Psi_\alpha^B\rangle$ appear in the spectral decomposition of the reduced density matrices (cf. Eq. (6))

$$\rho^A = \sum_\alpha p_\alpha |\Psi_\alpha^A\rangle\langle\Psi_\alpha^A|, \quad \rho^B = \sum_\alpha p_\alpha |\Psi_\alpha^B\rangle\langle\Psi_\alpha^B|, \tag{15}$$

and where the number of terms $\chi(A:B)$ in the decomposition, known as the Schmidt rank, can be used as a measure of entanglement between blocks $A$ and $B$.[59]

In Ref. 21 a canonical form for the TTN was proposed, where each bond index of the TTN corresponds to a Schmidt

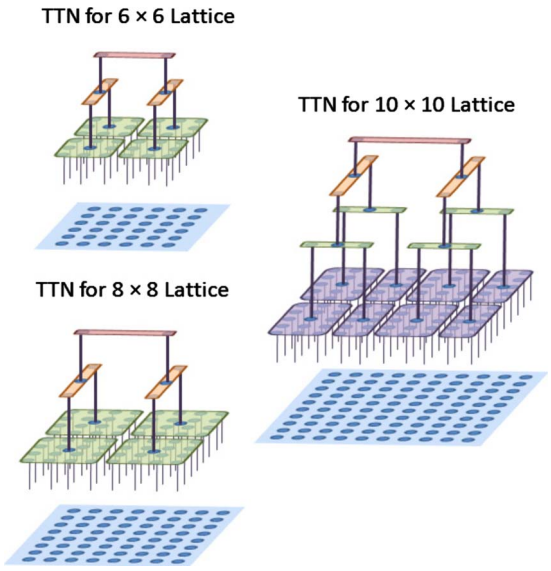


FIG. 5. (Color online) Isometric TTN for lattices of $6\times6$, $8\times8$, and $10\times10$ sites as used in the manuscript for the purpose of benchmarking the performance of the algorithm of Sec. IV. Notice that all TTN have the same structure on the two top layers of isometries, whose manipulation dominates the computational cost of the algorithm, while they differ in the lower layers. In particular, in the $10\times10$ lattice two lower layers of isometries are required since a single layer of isometries mapping a block of $5\times5$ sites directly into a single effective site would have been too expensive given the present capabilities of the desktop computers used for the simulations.

decomposition. That is, in its canonical form, a TTN can be regarded as a collection of Schmidt decompositions of a state according to a family of nested bipartitions $A:B$ of the system.

In this work we do not use the canonical form of a TTN. However, the use of isometric tensors implies that the rank of each bond index in our TTN is given by the Schmidt rank $\chi(A:B)$ of the corresponding partition. In particular, the bond dimension $\chi$ in Eq. (13) corresponds to the Schmidt rank between two halves of the system, as well as between one fourth and three fourths of the system.

### G. Symmetries

The symmetries of a state $|\Psi\rangle$ of the lattice $\mathcal{L}$ can often be incorporated to some extent into the TTN, resulting in a reduction on computational costs. One can distinguish between *space symmetries*, such as invariance under translations, e.g., by one lattice site or invariance under rotation of the lattice by, e.g., 90°, and *internal symmetries*, such as particle number conservation or spin isotropy.

The coarse-graining implicit in the TTN ansatz is incompatible with most space symmetries. As a result, a TTN approximation to a symmetric state typically breaks such symmetries. However, the symmetry is seen to be restored in the limit of a large $\chi$. In addition, the isometries can often explicitly incorporate part of the symmetry. For instance, in approximating states that are invariant under translations in $4\times4$, $6\times6$, or $8\times8$ lattices by using the TTNs of Figs. 1 and 5, one can choose all the isometries on a given layer of the TTN to be the same.

In contrast, internal symmetries can be implemented exactly in the TTN. Suppose for example that the state is known to have a well defined particle number [U(1) symmetry] or to be a singlet under spin rotations [SU(2) symmetry]. Then one can choose all the isometries of the tree to be covariant under the action of the symmetry, in such a way that: (i) the symmetry is preserved *exactly* by any value of $\chi$, and (ii) many parameters of the isometries are fixed by the symmetry, leading to a significant reduction in computational cost. We refer to Refs. 60–62 for more details. In the actual computations presented in this work we have not implemented internal symmetries in the TTN.

### H. Relation to real-space RG

Being based on coarse graining the lattice $\mathcal{L}$, the present approach is closely related to the real-space RG ideas and methods proposed by Kadanoff and co-workers.[24–29] The TTN ansatz can indeed be regarded as a specific implementation of the spin-blocking schemes that these authors put forward.

However, it is important to emphasize the differences between the present approach and those usually associated to real-space RG methods. First of all, here we attempt to obtain a quasiexact description of the ground state $|\Psi_{\mathrm{GS}}\rangle$ of a finite lattice $\mathcal{L}$, which forces us to consider effective sites with a dimension $\chi_\tau$ that grows (exponentially) with the number of iterations $\tau$ of the coarse-graining transformation. Instead, real-space RG approaches typically attempt to identify and characterize the fixed points of the RG flow on an infinite system and consider a fixed dimension $\chi_\tau$. A second important difference is in the way the isometries are chosen. Wilson proposed to consider the restriction $H_B$ of the Hamiltonian $H$ on a block of sites $B$, and to choose the isometries in order to preserve the subspace corresponding to the lowest energy eigenvalues of $H_B$. Here, instead, we aim at globally minimizing $H$ (see Sec. IV), thereby following the path initiated with White's DMRG.[36–38]

### I. Relation to MERA

The TTN ansatz considered in this work can also be thought of as a particular case of the MERA, see Refs. 12–15. Specifically, a MERA where disentanglers are replaced with identity operators becomes a TTN. We emphasize that the manipulations of a TTN, as discussed in Secs. III and IV, are different than those for the MERA. Indeed, the absence of disentanglers changes the optimal pattern of tensor network contractions. As a result, for instance, the scaling of the computational cost with $\chi$ is much smaller with a TTN [namely, $\mathcal{O}(\chi^4)$] than with a MERA.[14] Of course, for large 2D lattices the benefits of having a cost that scales as a smaller power of $\chi$ are offset by the need to use a much larger value of $\chi$, and simulations with a TTN become more expensive than with the MERA.

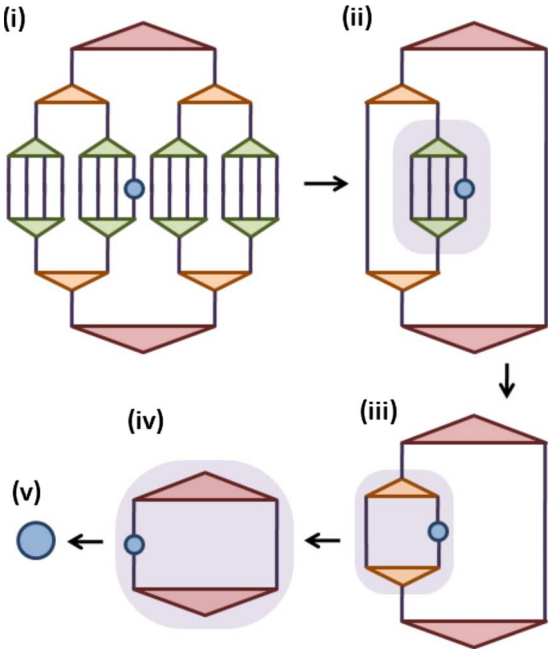


FIG. 6. (Color online) Computation of the expectation value $\langle\Psi|o^{[s]}|\Psi\rangle$ of a one-site operator $o^{[s]}$ acting on site $s \in \mathcal{L}$. (i) Tensor network to be contracted. (ii) Tensor network left after many of the isometries are annihilated by their Hermitian conjugate, see Fig. 2. After the steps from (iii) to (v) the expectation value is obtained.

## III. COMPUTATION OF LOCAL OPERATORS, FIDELITIES, AND ENTROPIES

In this section we assume that a TTN for the state $|\Psi\rangle$ of an $L\times L$ lattice $\mathcal{L}$ has been provided, and explain how to extract a number of quantities of interest from it. This section is presented before explaining the optimization algorithm in the next section mostly for two reasons. On the one hand, the algorithm of Sec. IV is only one of many possible ways of obtaining a TTN (one could alternatively consider using a different optimization algorithm,[18–22] or obtain a TTN through an analytical derivation)[16,17] and yet in all cases it is still necessary to extract information from the TTN representation. On the other hand, by explaining now how to compute quantities of interest from a TTN, we also introduce material that will be useful later on in order to understand the optimization algorithm.

### A. Expectation value of local operators, two-point correlation functions, and fidelity

We start by noticing that since the TTN is made of isometries, the state $|\Psi\rangle$ it represents is automatically normalized, $\langle\Psi|\Psi\rangle=1$.

Given a local operator $o^{[s]}$ that acts on a single-site $s$ of $\mathcal{L}$, the expectation value

$$\langle\Psi|o^{[s]}|\Psi\rangle, \tag{16}$$

can be computed by contracting the tensor network of Fig. 6. Notice that an important fraction of the isometries in the TTN are annihilated by their Hermitian conjugate pair, see Fig. 2, and are therefore not involved in the computation of $\langle\Psi|o^{[s]}|\Psi\rangle$.

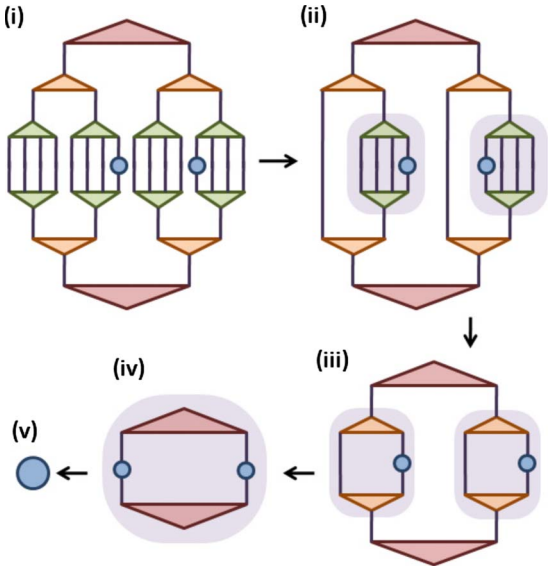


FIG. 7. (Color online) Computation of the expectation value $\langle\Psi|o^{[s]}o^{[s']}|\Psi\rangle$ corresponding to a two-site correlation function. (i) Tensor network to be contracted. (ii) Tensor network left after several isometries are annihilated by their Hermitian conjugate. After the steps from (iii) to (v) the expectation value is obtained.

A local operator $o^{[ss']}$ that acts on two sites $s$ and $s'$ of $\mathcal{L}$ can always be decomposed as a sum of products of one-site operators $o_\alpha^{[s]}$ and $o_\beta^{[s']}$,

$$o^{[ss']}=\sum_{\alpha\beta} o_\alpha^{[s]}o_\beta^{[s']}. \tag{17}$$

Therefore, without loss of generality we can concentrate on the calculation of a two-point correlation function

$$\langle\Psi|o^{[s]}o^{[s']}|\Psi\rangle. \tag{18}$$

This computation is achieved by contracting the tensor network of Fig. 7. A minor difference with the previous contraction for a single-site operator is that now less pairs of isometries are annihilated.

More generally, the expectation value of a product of $p$ one-site operators $\langle\Psi|o^{[s_1]}o^{[s_2]}\cdots o^{[s_p]}|\Psi\rangle$ can also be obtained by contracting a similar tensor network, and so can the overlap or fidelity $\langle\Psi_1|\Psi_2\rangle$ between two states $|\Psi_1\rangle$ and $|\Psi_2\rangle$ represented by a TTN with equivalent tree structure, see Fig. 8.

### B. Spectrum and entropy of the reduced density matrix of a block of sites

Finally, from the TTN it is straightforward to compute the spectrum $\{p_\alpha\}$ of the reduced density matrix $\rho^A$ [cf. Eq. (6)] for certain blocks $A$ of sites, namely, those that correspond to an effective site of any of the coarse-grained lattices $\mathcal{L}_1,\ldots,\mathcal{L}_{T-1}$. Figure 9 illustrates the tensor network corresponding to $\rho^A$ for the case when $A$ is one half of the lattice. As before, many pairs of isometries are annihilated. In addi-

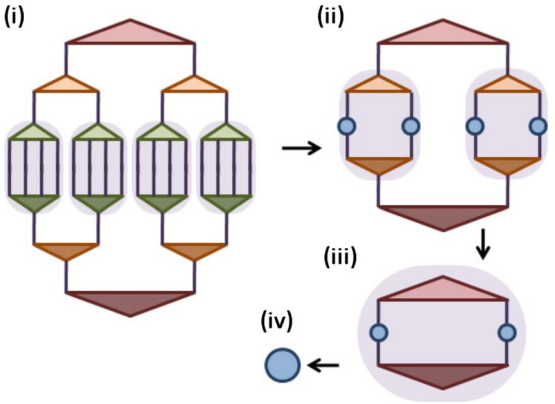


FIG. 8. (Color online) Computation of the overlap or fidelity $\langle\Psi_1|\Psi_2\rangle$ between two states $|\Psi_1\rangle$ and $|\Psi_2\rangle$ each represented with a TTN. (i) Tensor network corresponding to $\langle\Psi_1|\Psi_2\rangle$. Notice that in this case no isometry is annihilated, since the isometries of the two TTNs are not the same. After the steps from (ii) to (iv) the overlap or fidelity is obtained.

tion, the isometries contained within region $A$ can be removed since they do not affect the spectrum of $\rho^{[A]}$. From the spectrum $\{p_\alpha\}$, we can now obtain the entropy $S(A)$ of Eq. (7).

In the large $\chi$ regime, where the bond dimension at the top layers of the TTN is much larger than in the lowest layers, the cost of contracting any of the tensor networks in Fig. 6–9 is dominated by matrix multiplications whose computational cost scales as $\chi^4$. Thus, this is the cost of all the tasks discussed in this section.

## IV. OPTIMIZATION ALGORITHM

In this section we describe an algorithm to optimize the TTN ansatz so that it approximates the ground-state $|\Psi_{\rm GS}\rangle$ of a Hamiltonian $H$,

$$H|\Psi_{\rm GS}\rangle = E_{\rm GS}|\Psi_{\rm GS}\rangle, \tag{19}$$

defined on an $L\times L$ lattice $\mathcal{L}$ with torus topology. For simplicity we will assume that the Hamiltonian $H$ decomposes

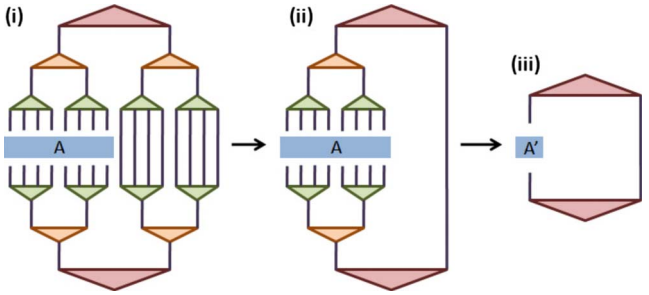


FIG. 9. (Color online) Computation of the spectrum $\{p_\alpha\}$ of the reduced density matrix $\rho^A$ for a block $A$ that corresponds to one of the coarse-grained sites. (i) Tensor network corresponding to $\rho^A$ where $A$ is half of the lattice. (ii) Tensor network left after several isometries are annihilated with their Hermitian conjugate. (iii) since the spectrum of $\rho^{[A]}$ is not changed by the isometries acting on $A$, we can also eliminate those isometries and we are left with a network consisting of only two tensors, which can now be contracted together.

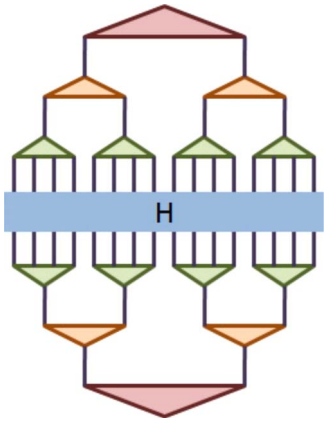


FIG. 10. (Color online) Tensor network corresponding to the cost function $E(\{w_i\})=\langle\Psi_{\{w_i\}}|H|\Psi_{\{w_i\}}\rangle$ to be minimized.

into two-site terms that couple only pairs of nearest-neighbor sites $s,s'\in\mathcal{L}$,

$$H = \sum_{\langle s,s'\rangle} h^{[s,s']}, \tag{20}$$

although much more complicated Hamiltonians (e.g., with plaquette interactions or arbitrarily long-range interactions) can be also considered with only minor modifications of the algorithm.

### A. Cost function and optimization strategy

Given the TTN ansatz $|\Psi_{\{w_i\}}\rangle$ at a fixed value of $\chi$, our goal is to minimize the expectation value

$$E(\{w_i\}) \equiv \langle\Psi_{\{w_i\}}|H|\Psi_{\{w_i\}}\rangle, \tag{21}$$

as represented in Fig. 10, by optimizing all the isometries $\{w_i\}$ in the TTN, so as to obtain an optimal approximation $E(\{\bar{w}_i\})$ to the ground state energy $E_{\rm GS}$,

$$E(\{\bar{w}_i\}) \equiv \min_{\{w_i\}}\langle\Psi_{\{w_i\}}|H|\Psi_{\{w_i\}}\rangle, \tag{22}$$

as well as an optimal TTN approximation $|\Psi_{\{\bar{w}_i\}}\rangle$ to the ground-state $|\Psi_{\rm GS}\rangle$.

An *exact* solution to Eq. (22) is not known. However, one may attempt to *approximately* minimize the energy $E(\{w_i\})$ in many different ways. Here we will do so by means of an iterative optimization strategy, which is an adaptation to the present context of the algorithm described in Ref. 15.

Starting with some set of initially random isometries $\{w_1,w_2,w_3,\cdots\}$, we will first optimize one of them, say, $w_1$, to obtain an optimal $w_1'$. Then, given the updated set $\{w_1',w_2,w_3,\ldots\}$, we will optimize another isometry, say $w_2$, obtaining $w_2'$. In the next step, given the updated set $\{w_1',w_2',w_3,\cdots\}$, yet another isometry will be optimized, and so on, until we have optimized all the isometries in the TTN. This defines one sweep. Then the sweep is iterated a number of times, until the cost function $E(\{w_i\})$ is seen to converge according to some criterion, for instance until it does not change between sweeps by more than some small amount.

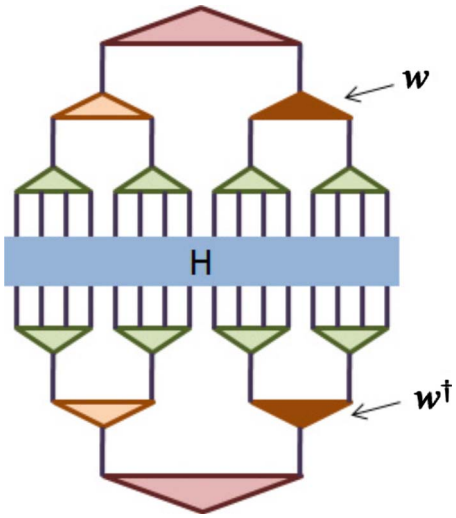


FIG. 11. (Color online) Tensor network representation for the cost function $E(w)=F(w)+G$ in Eq. (25) depending only on one isometry $w$.

### B. Optimization of an isometry

Next we explain how, given a set of isometries $\{w_i\}$ for the TTN at some stage of the minimization procedure, one can optimize one isometry $w$. Recall that $w$ is associated to a block $A$ of sites of $\mathcal{L}$.

First we notice that the cost function $E(\{w_i\})$ decomposes as a sum of two-site contributions

$$E(\{w_i\}) = \sum_{\langle s,s'\rangle} E^{ss'}(\{w_i\}), \tag{23}$$

$$\equiv \sum_{\langle s,s'\rangle} \langle \Psi_{\{w_i\}} | h^{[s,s']} | \Psi_{\{w_i\}} \rangle. \tag{24}$$

From now on, we also assume for simplicity in the explanation that $h^{[s,s']}$ is the product of two one-site operators. (If it is not, we can always decompose $h^{[s,s']}$ as a sum of such products.)

When viewed as a function of $w$ only, Fig. 11, $E(\{w_i\})$ can be divided into two pieces,

$$E(w) = F(w) + G. \tag{25}$$

Here $F(w)$ collects all two-site contributions $E^{ss'}$ where at least one of the two sites $s,s \in \mathcal{L}'$ are included in the block $A$ associated to $w$, and $F$ collects the rest of two-site contributions, see Fig. 12. Notice that if both $s$ and $s'$ in $E^{ss'}$ lie outside the block $A$, then the pair $w$ and $w^\dagger$ cancels out due to Eq. (2), and $E^{ss'}$ does not depend on $w$. Therefore, $G$ is independent of $w$ and we can focus on minimizing $F(w)$. In turn, $F(w)$ can also be divided into two pieces,

$$F(w) = F^{AA}(w) + F^{AB}(w), \tag{26}$$

where $F^{AA}(w)$ collects all contributions $E^{ss'}$ with both sites $s$ and $s'$ in $A$, whereas $F^{AB}(w)$ corresponds to the terms $E^{ss'}$ that include one site in $A$ and the other site in its complementary $B$ [cases (i) and (ii) of Fig. 12]. The optimization

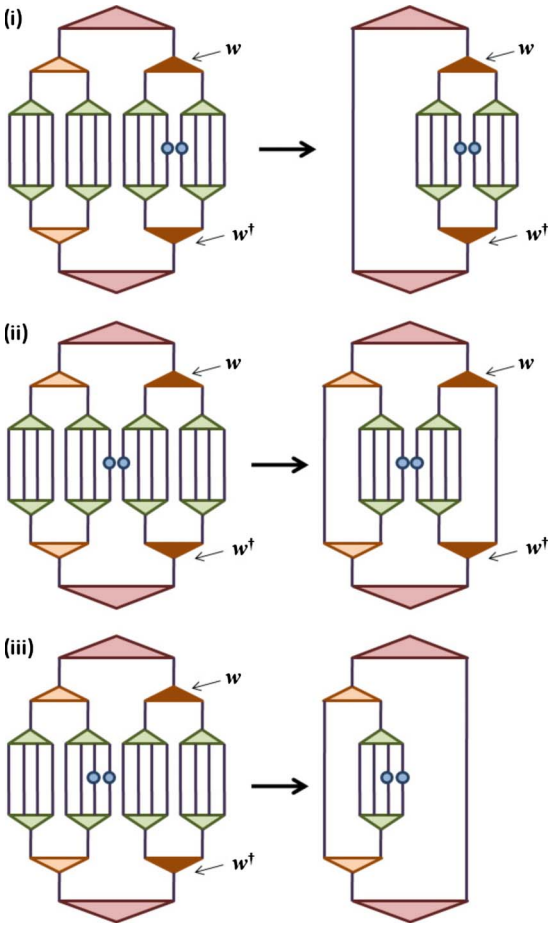


FIG. 12. (Color online) Examples of the three different types of two-site terms $E^{ss'}$ contributing to $E(w)$: in (i) both $s$ and $s'$ are contained within the block $A$ associated to $w$; in (ii) only one of the sites, say $s$, belongs to $A$; finally in (iii) both sites $s$ and $s'$ are outside $A$. The terms (i) and (ii) contribute to $F^{AA}(w)$ and $F^{AB}(w)$ in Eq. (26), respectively, whereas the term (iii) contributes to the constant $G$ in 25.

$$\min_w F(w), \tag{27}$$

is bilinear in $w,w^\dagger$ and is subject to the isometric constraint of Eq. (2). Unfortunately, once more we do not know how to solve this minimization exactly.

Following Ref. 15, we will approximately minimize $F(w)$ as follows. First we linearize $F(w)$ by considering $w$ to be independent of $w^\dagger$, and then we minimize the resulting cost function $I(w)=\mathrm{tr}(\Upsilon w)$,

$$\min_w I(w) = \min_w \mathrm{tr}(\Upsilon w), \tag{28}$$

where $\Upsilon$ is the *environment* of $w$. The function $I(w)$ can be minimized exactly, with the optimal solution corresponding to $w'=-VU^\dagger$, where $\Upsilon=USV^\dagger$ is the singular value decomposition of $\Upsilon$.

Once we have obtained the optimal $w'$, we can replace $w^\dagger$ with $w'^\dagger$ in $F(w)$, resulting in an updated environment $\Upsilon'$ that we use to minimize $I(w)$ again. Iteration produces a sequence of isometries $\{w,w',w'',\ldots\}$ that typically lead to

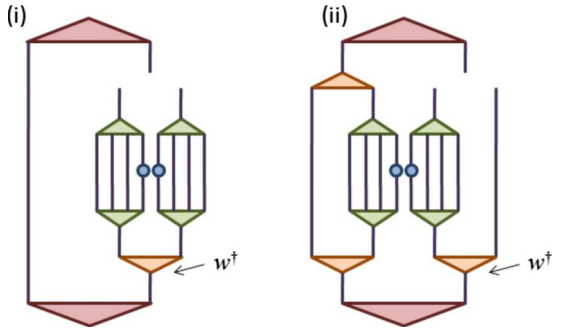


FIG. 13. (Color online) Examples of the two different types of two-site terms that contribute to the environment $\Upsilon$ for the isometry $w$: (i) both $s$ and $s'$ are contained within the block $A$ associated to $w$, and therefore this term contributes to $\Upsilon^{AA}$; (ii) only one of the sites, say, $s$, belongs to $A$ and therefore this term contributes to $\Upsilon^{AB}$.

monotonically decreasing values of the cost function, that is $F(w) \geq F(w') \geq F(w'') \geq \cdots$. One could in principle iterate the minimization of $F(w)$ until some level of convergence has been reached. However, in practice we only use a small number of iterations (even just one) before moving to optimize another isometry of the TTN, since in actual simulations this is seen to be already enough to perform the minimization of Eq. (22). The order in which the isometries are optimized does not seem to play a relevant role in the performance of the algorithm.

All that is left is to explain how to compute the environment $\Upsilon$ of an isometry. Again, the environment breaks into two-site contributions corresponding to the terms $E^{ss'}$ that appear in $F^{AA}(w)$ and $F^{AB}(w)$,

$$\Upsilon = \Upsilon^{AA} + \Upsilon^{AB}. \tag{29}$$

Figure 13 shows examples of two-site contributions to $\Upsilon^{AA}$ and $\Upsilon^{AB}$.

The cost of optimizing an isometry comes from the computation of the environment $\Upsilon$ and from its singular value decomposition. These costs depend on which isometry $w$ is optimized, but the cost of sweeping over all the isometries of a given layer of the TTN can be seen to scale as $O(L\chi^4)$, since there are $O(L)$ Hamiltonian terms $h^{[ss']}$ at the boundary between two halves of the system and computing the associated contribution to an environment $\Upsilon$ has a cost $\chi^4$. (Notice that the singular value decomposition of the environments $\Upsilon$ for the two largest isometries also costs $\chi^4$). Therefore the leading order (in $\chi$) of the cost of sweeping over the whole tree scales as $O(L\chi^4)$, and is also proportional to the number of layers in the TTN. In a translation invariant setting where all the isometries in a layer of the TTN can be chosen to be the same, this leading cost still scales as $O(L\chi^4)$ and remains proportional to the number of layers, but it has a reduced multiplicative prefactor. In a lattice of $8 \times 8$ sites, a typical computation of the ground state (where optimization of isometries proceeds until the expectation value of the energy does not change by more than $10^{-10}$ per sweep) requires of the order of 100–500 sweeps.

In the case of a Hamiltonian made of long-range two-site interactions, where all sites interact with all sites, the number of Hamiltonian terms $h^{[ss]}$ grows as $O(L^4)$ and, correspondingly, the overall cost of sweeping over the whole tree scales as $O(L^4\chi^4)$.

## V. BENCHMARK RESULTS

In order to test the usefulness of the TTN ansatz and to benchmark the performance of the optimization algorithm, we consider the quantum Ising model with transverse magnetic field, as given by the Hamiltonian

$$H_{\text{Ising}} = -\sum_{\langle ss' \rangle} \sigma_x^{[s]} \otimes \sigma_x^{[s']} - \lambda \sigma_z^{[s]}, \tag{30}$$

where $\sigma_x$ and $\sigma_z$ are Pauli matrices and $\lambda$ is the magnitude of the transverse magnetic field. We consider a square lattices made of $L \times L$ sites and with toroidal boundary conditions. Since each site corresponds to a spin-1/2 degree of freedom, its vector space dimension is $d=2$. In the thermodynamic limit, the model is known to undergo a quantum phase transition at a value of the transverse magnetic field $\lambda_c \approx 3.044$.[63,64]

We have computed TTN approximations to the ground state of $H_{\text{Ising}}$ in lattices of linear size $L=\{4,6,8,10,16,32\}$ and for several values of $\chi \leq 500$. Exploiting translation invariance, we have chosen, on each layer of the TTN, all isometries to be the same. For $L \leq 8$ we are in a *quasiexact regime* where results appear to be very accurate, whereas for $L \geq 10$ we are in an *approximate regime* where the results are not yet converged with respect to $\chi$, but it is still possible to obtain qualitatively correct results.

### A. Quasiexact regime

For $L=4,6,8$ we have computed approximations to the ground state of $H_{\text{Ising}}$ for values of the transverse magnetic fields in the range $\lambda \in [1,5]$. Figures 14 and 15 show the expectation values for the interaction per link,

$$\langle \sigma_x \sigma_x \rangle \equiv \frac{1}{2N} \sum_{\langle s,s' \rangle} \langle \sigma_x^{[s]} \sigma_x^{[s']} \rangle, \tag{31}$$

and the transverse magnetization per site

$$\langle \sigma_z \rangle \equiv \frac{1}{N} \sum_{s} \langle \sigma_z^{[s]} \rangle, \tag{32}$$

in terms of which the energy per site reads

$$e \equiv \frac{1}{N} \langle H \rangle = -2 \langle \sigma_x \sigma_x \rangle - \lambda \langle \sigma_z \rangle. \tag{33}$$

Both observables in Figs. 14 and 15 around $\lambda \simeq 3$ have a very steep dependence on $\lambda$. This behavior is consistent with the presence of a phase transition at $\lambda = 3.044$ (in order to find the precise location of the transition point one should perform a finite-size scaling analysis. However, at least in its simplest version,[1,65] a finite-size scaling analysis requires knowledge of the energy gap between the ground state and first-excited state of $H$. While this gap can in principle be computed with a TTN, such computation is beyond the scope

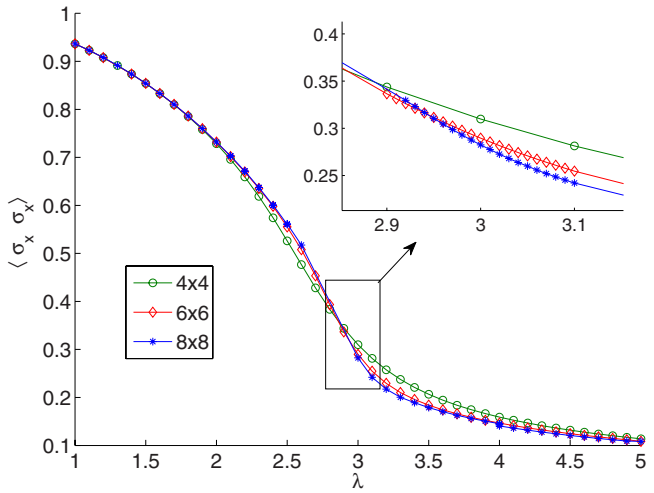


FIG. 14. (Color online) Expectation value $\langle\sigma_x\sigma_x\rangle$ as a function of the transverse magnetic field $\lambda$ and for lattices of $4\times4$, $6\times6$, and $8\times8$ sites. Notice that, as the lattice size grows, $\langle\sigma_x\sigma_x\rangle$ becomes steeper and less smooth around $\lambda\approx3$, consistent with the existence of a critical point at $\lambda_c\approx3.044$ in the thermodynamic limit (Refs. 63 and 64).

of the present work, restricted to ground states) as determined in Refs. 63 and 64.

In order to assess the accuracy of our numerical results, we first compare the expectation value of the energy with its exact value, as obtained in Ref. 1 using exact diagonalization techniques on a $6\times6$ lattice. (Notice that $6\times6$ is the largest $L\times L$ lattice that can be addressed with exact diagonalization). For $\lambda=3.05266$ (and thus near the critical point) the exact value of the energy per site as obtained in Ref. 1 is $e=-3.247\,274\,397\,58\cdots$. Figure 16 shows the error in the energy per site obtained with a TTN with $\chi$ ranging from 100 to 550. This error is of the order of $10^{-4}$ for $\chi=100$ and

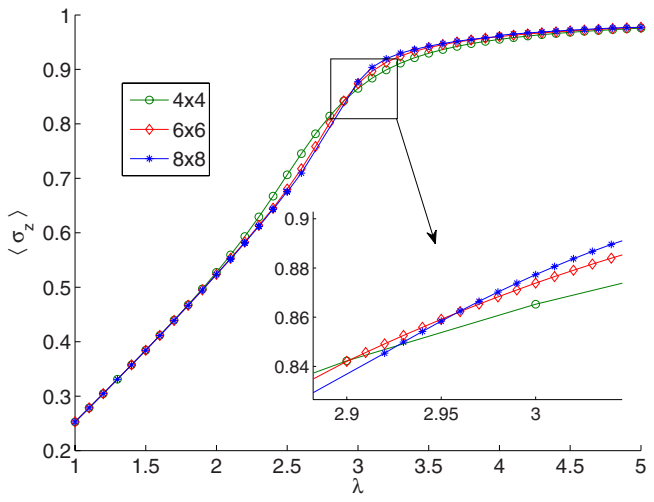


FIG. 15. (Color online) Expectation value $\langle\sigma_z\rangle$ for the transverse magnetization as a function of the transverse magnetic field $\lambda$ and for lattices of $4\times4$, $6\times6$, and $8\times8$ sites. Again, as the lattice size grows $\langle\sigma_z\rangle$ becomes steeper and less smooth around $\lambda\approx3$, consistent with the existence of a critical point at $\lambda_c\approx3.044$ in the thermodynamic limit (Refs. 63 and 64).

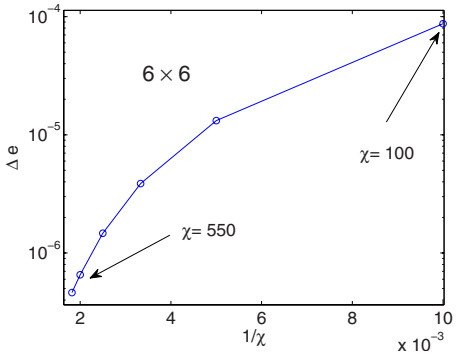


FIG. 16. (Color online) Error of the ground state energy per site $\Delta e\equiv e(\chi)-e_{exact}$ [cf. Eq. (33)] for a $6\times6$ lattice plotted as a function of $1/\chi$ at $\lambda=3.052\,66$. $\chi$ varies in the range from $\chi=100$ to $\chi=550$. $e_{exact}$ is extracted from Ref. 1. In the plot we see that $\Delta e$ ranges from $\Delta e\sim\mathcal{O}(10^{-4})$ in the case of $\chi=100$ to $\Delta e\sim\mathcal{O}(10^{-7})$ in the case of $\chi=550$. All the TTN simulations used here require much smaller computational resources than the full exact diagonalization calculation as we explain in detail in the main text.

under $3\times10^{-7}$ for $\chi=550$. In the first case, the computation lasts 20 min on a standard PC and uses less than 0.5 Gbyte of random access memory (RAM). In the latter case, the simulation takes around 2 days and uses about 8 Gbyte of RAM. By comparison, the computation by exact diagonalization required 35 Gbyte of RAM.[1]

This means that, for the model we are considering, we obtain accurate results with a fraction of the resources needed by the exact diagonalization algorithms.

For larger lattices we do not have exact results to compare against. In this case we study the convergence in $\chi$ of the energy per site $e$ for a value $\lambda=3.05$ of transverse magnetic field close to the critical value $\lambda_c$. This regime is the hardest to simulate, since ground states are most entangled at criticality. As shown in Fig. 17, where we plot the energy per site $e$ and its deviation $\Delta e\equiv e(\chi)-e(\chi_{max})$ from our best estimate $e(\chi_{max})$, for values of $\chi$ around 500, $e$ depends only very weakly on $\chi$. The figure also shows that, as expected, the $6\times6$ case converges faster with large $\chi$ than the $8\times8$ case. Notice that, bigger systems have higher energies per site, in agreement with previous finite-size scaling studies.[1]

Further evidence in favor of convergence of the results in an $8\times8$ lattice with $\chi$ is obtained by studying the spectrum of the reduced density matrix for one half of the lattice. In Fig. 18 we have plotted the largest 200 eigenvalues of this spectrum, again for $\lambda=3.05$. We see that in changing $\chi$ from 200 to 500 in our energy optimization, the upper part of the spectrum remains essentially unchanged. Also, the spectrum $\{p_\alpha\}$ decays very fast as a function of $\alpha$ presenting only around 50 eigenvalues larger than $10^{-4}$. This also implies that typical errors in the expectation value of observables should be very small (we will provide examples of this statement in the section on the entropies). The study of the spectrum of one half of the lattice as a function of $\lambda$, as displayed in Fig. 19, confirms that the ground state is most entangled, and therefore its computation most challenging, for $\lambda$ around $\lambda_c$. It is also interesting to notice that, for magnetic fields $\lambda$ smaller than the critical $\lambda_c$, the spectrum presents a very peculiar plateaux structure that will be analyzed in detail in the next section.

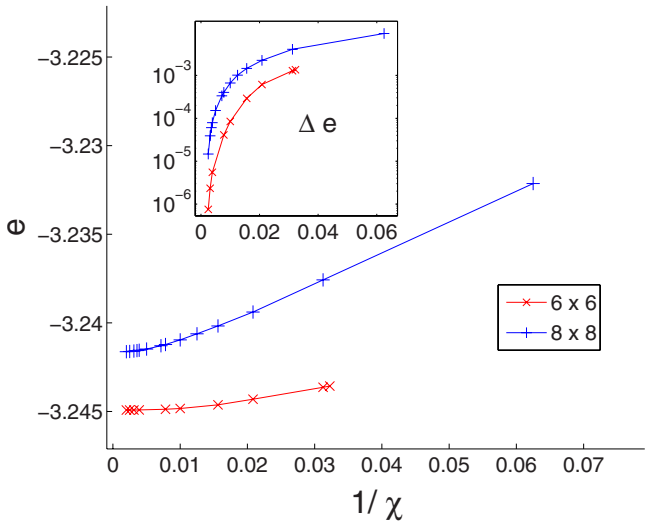


FIG. 17. (Color online) Approximate ground state energy per site $e$ [cf. Eq. (33)] for $\lambda=3.05$ plotted as a function of $1/\chi$, for lattices of $6\times6$ and $8\times8$ sites. Notice that in both cases the results seem to have converged for large $\chi$ up to several digits of accuracy. The insets show the difference $\Delta e \equiv e(\chi)-e(\chi_{max})$, as a function of $1/\chi$.

The structure of the TTN manifestly breaks translation and rotation invariance and it is natural to ask to what degree this affects the structure of correlations in the ansatz. Figure 20 shows the two-point correlation function

$$C(x,y) \equiv \langle \sigma_x^{[0,0]} \sigma_x^{(x,y)} \rangle, \tag{34}$$

where $(x,y)$ is a vector of integers indicating the position of a lattice site. Results obtained for a $8\times8$ lattice with just $\chi=100$ hardly show any difference between the correlation

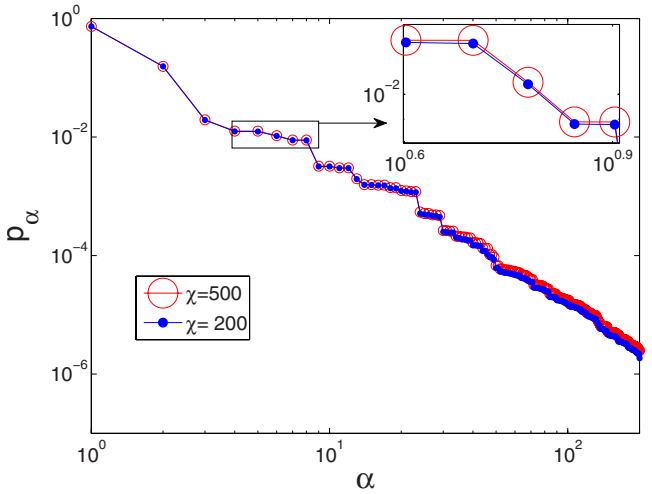


FIG. 18. (Color online) Spectum $\{p_\alpha\}$ for the reduced density matrix $\rho$ of one half of the lattice. The results the ground state of $H_{\text{Ising}}$ for $\lambda=3.05$ in a $8\times8$ lattice. Notice the relatively fast decay of the spectrum, with, e.g., $p_\alpha<10^{-4}$ for $\alpha>50$. Also, calculations with $\chi=200$ and $\chi=500$ produce spectra that are very similar for small $\alpha$. This is an indication that the largest eigenvalues ($p_\alpha$ for small $\alpha$) are already very close to their exact value.

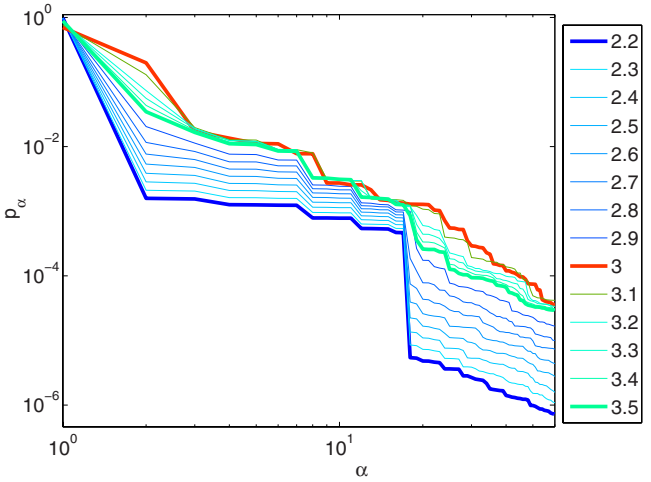


FIG. 19. (Color online) Spectrum of the reduced density matrix for one half the $8\times8$ lattice for different values of $\lambda$. The calculations, conducted with $\chi=100$, show that the spectrum decays slowest for $\lambda$ near $\lambda_c$. It also shows that for magnetic fields smaller than $\lambda_c$, the spectrum develops a clear structure of plateaux.

functions in the $x$ and $y$ directions. This seems to indicate that the space symmetries expected in the ground state have already been restored at a relatively small value of $\chi$.

The results in this section demonstrate that, for the model under consideration, the TTN approach offers a reliable route, based on exploiting the entropic area law, to extend the domain of quasiexact results well beyond what is possible using exact diagonalization techniques.[1]

### B. Approximate regime

For lattices of linear size $L\geq10$ we no longer obtain convincingly converged results for $\chi\approx500$ when trying to approximate the ground state of $H_{\text{Ising}}$ for $\lambda$ close to $\lambda_c$. Interestingly, however, we still obtain reasonably converged results for a large range of $\lambda$ away from $\lambda_c$, which in the case of a $10\times10$ lattice allows us to obtain qualitatively the whole phase diagram of the system, see Figs. 21 and 22.

More generally, we find that converged results for lattices as large as $L=16$ and $L=32$ can be obtained, with $\chi\leq500$, for values of $\lambda$ not too distant from $\lambda_c$. This can be explained by the presence of a plateaux structure in the spectrum of the reduced density matrix of one half of the lattice, see Fig. 23. The first plateau consists of exactly $2L$ eigenvalues $p_\alpha$, that is $\alpha\in[2,2L+1]$. The second plateau is much larger, but its eigenvalues are often already very small. For instance, for $\lambda=2.4$, the first plateau corresponds to $p_\alpha\approx10^{-3}$, whereas in the second plateau to $p_\alpha\approx10^{-5}-10^{-6}$. Importantly, Fig. 24 shows that simulations with a value of $\chi$ slightly above $2L$ can already accurately reproduce the first plateau and obtain a reasonable approximation to the ground state of the system. This can be explained using perturbation theory as done, e.g., in Sec. IIIB in Ref. 45.

### C. The exponential cost

We have seen that the presence of plateaux in the spectra of reduced density matrices can reduce the cost for an ap-

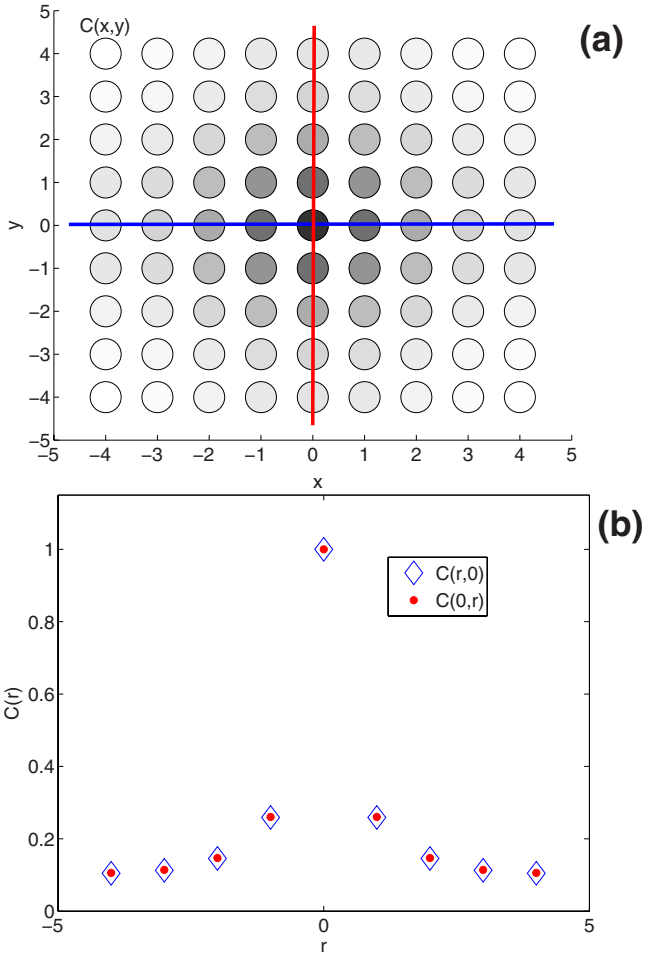


FIG. 20. (Color online) Two-point correlation functions $C(x,y)$ of Eq. (34) for the ground state of $H_{\text{Ising}}$ with transverse magnetic field $\lambda=3.05$. The correlation function between distant points in the torus remain large, as one would expect of a system that becomes critical in the thermodynamic limit. The results, obtained with a TTN with $\chi=100$, show that the invariance of the system under 90° rotations is preserved, in spite of the fact that the TTN manifestly breaks it at its top layers. Indeed, one can hardly distinguish $C(r,0)$ from $C(0,r)$.

proximate description of ground states with a TTN to a linear function in the size of the system. In general, however, such short plateaux are not expected (see, e.g., the valence-bond crystal example given in Sec. II C). In particular, close to the critical point, we do not observe any plateaux. We have repeatedly stated that a faithful representation of the ground state with a TTN in this regime requires an exponential cost in the size of the system. Here we make this statement more precise. In order to achieve this we study how the rank of the TTN $\chi$ should increase to keep the error in the energy (as an example of a local observable) constant as we increase the system size. The error in the energy is estimated from our numerical data as

$$\Delta e(\chi) \equiv e_{\chi} - e_{\chi_{max}}, \tag{35}$$

where $e_{\chi_{max}}$ is our best available result.

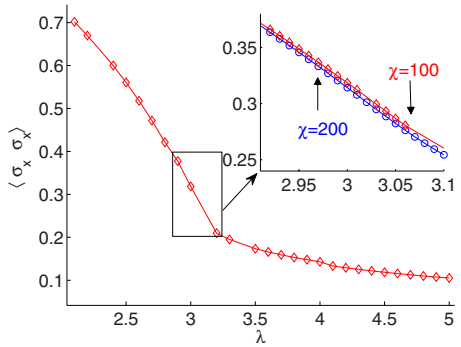


FIG. 21. (Color online) Expectation value $\langle\sigma_x\sigma_x\rangle$ as a function of the transverse magnetic field $\lambda$ and for a $10\times10$ lattice. The inset shows results obtained with $\chi=100$ and $\chi=200$ for values of the transverse magnetic field $\lambda$ close to $\lambda_c$. In this approximate regime, the TTN algorithm produces results that are not converged with respect to $\chi$ near the quantum critical point.

For each system size $L$ we denote by $\chi_\varepsilon(L)$ the minimum $\chi$ that leads to at most an error $\varepsilon$ in the energy. This procedure is illustrated in Fig. 25. In turn, Fig. 26 displays the value of $\chi_\epsilon(L)$ as a function of $L$. It shows that $\chi_\epsilon(L)$ grows exponentially with $L$ for large $L$, thereby confirming that the cost of faithfully representing the ground state with a TTN increases exponentially with the linear size of the system.

### D. Error analysis

The TTN is a variational ansatz whose precision can be improved by increasing the value of the refinement parameter $\chi$. Ideally, for very large $\chi$, the results should become exact. A precise theory on how to detect this asymptotic regime is beyond the scope of this work. However we see that several observables $\mathcal{O}=\langle\Psi_\chi|O|\Psi_\chi\rangle$ converge to their large $\chi$ value in a characteristic way. Namely, $\mathcal{O}(1/\chi)$ is a monotonic function of $1/\chi$ with positive, monotonically increasing derivative. For such observables, a rough estimate of the error induced by using a finite value of $\chi$ can be obtained as follows. The monotonic nature of $\mathcal{O}$ ensures that $\mathcal{O}(1/\chi_{max})>\mathcal{O}(0)\equiv\mathcal{O}_{exact}$. With a linear fit to the behavior of $\mathcal{O}(1/\chi)$ close to $1/\chi_{max}$ we can extrapolate $\mathcal{O}$ to $1/\chi=0$

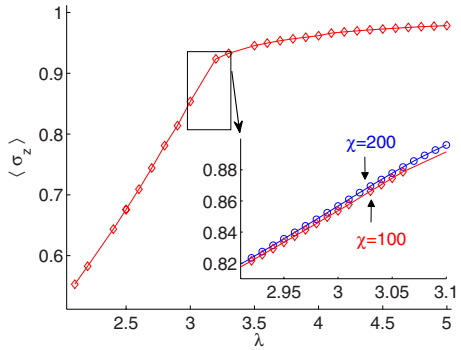


FIG. 22. (Color online) Expectation value $\langle\sigma_z\rangle$ as a function of the transverse magnetic field $\lambda$ and for a $10\times10$ lattice. The inset shows results obtained with $\chi=100$ and $\chi=200$ for values of the transverse magnetic field $\lambda$ close to $\lambda_c$.

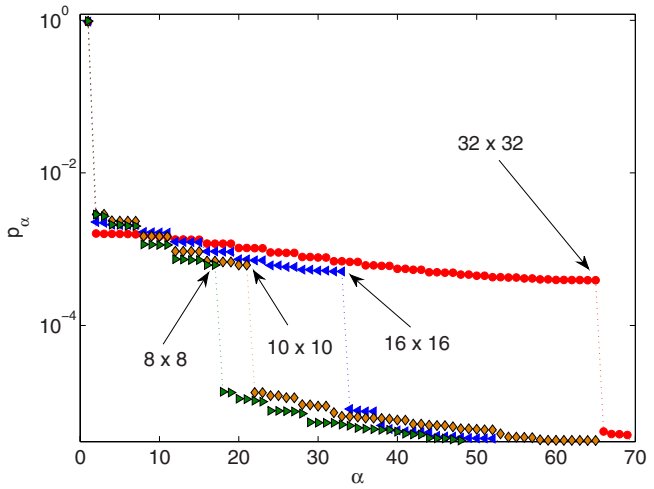


FIG. 23. (Color online) Spectrum $\{p_\alpha\}$ of the reduced density matrix for one half of a $L\times L$ lattice in the ground state of $H_{\text{Ising}}$ for $\lambda=2.4$. These results, obtained with only $\chi=100$, show the presence of a plateau of exactly $2L$ eigenvalues $p_\alpha$, separated by two or more orders of magnitude from those of the next plateau. The structure of plateaux can be understood as a perturbative version of the entropic area law and explains why a TTN with relatively small $\chi$ can still produce converged results away from the critical point for large lattices $L\approx 10-30$. For a related discussion see also the Sec. IIIB in Ref. 45.

and obtain $\mathcal{O}_{low}$. Indeed, the conjectured properties of the derivative of $\mathcal{O}$ ensure that $\mathcal{O}_{low}\leq\mathcal{O}_{exact}$. In this way we manage to bound the exact solution with data available from the numerical simulations

$$\mathcal{O}_{low}\leq\mathcal{O}_{exact}\leq\mathcal{O}(1/\chi_{max}). \tag{36}$$

As important examples we consider in Fig. 27 the behavior of both the ground state energy and (minus) the entanglement entropy of the reduced density matrix of half the torus, for the critical Ising Model on a $4\times 4$ lattice. There, we can rely on exact diagonalization results and check that $|\mathcal{O}(1/\chi_{max})-\mathcal{O}_{low}|$ is an upper bound to the error induced by considering smaller $\chi$ than the one required by the exact solution. In this way we have estimated the errors appearing in the following section.

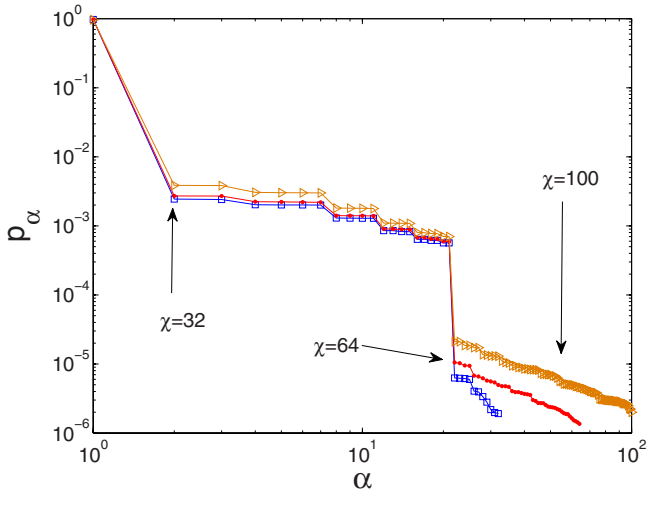


FIG. 24. (Color online) Spectrum $\{p_\alpha\}$ of one half of a $10\times 10$ lattice in the ground state of $H_{\text{Ising}}$ for $\lambda=2.4$. Results obtained with $\chi=32$, 64 and 100 do not differ significantly in the first 21 eigenvalues. This shows that the presence and composition of the first plateau of $2L$ eigenvalues of Fig. 23 (with $L=10$ in this case) is robust with respect to $\chi$.

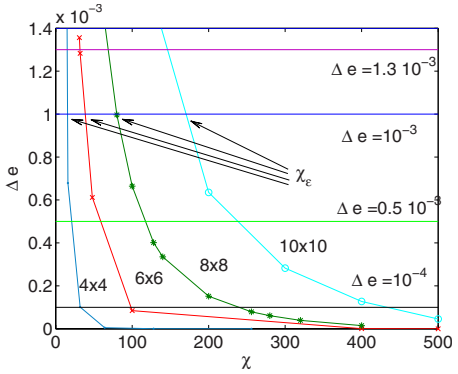


FIG. 25. (Color online) Plot of $\Delta e$ defined in Eq. (35) for torus of sizes $L=\{4,6,8,10\}$ and various $\chi$. We present several choices of $\varepsilon$ in the range $10^{-4}\leq\varepsilon\leq 1.3\times 10^{-3}$ represented by horizontal lines of different colors. The arrows identify the $\chi_\varepsilon$ defined in the text for the particular choice of $\varepsilon=10^{-3}$.

## VI. APPLICATION: ENTROPIC AREA LAW

The study of the entanglement entropy for the ground states of 2D quantum systems has been the subject of several recent works.[47–54] The TTN approach provides a natural scenario for these studies.

### A. Entanglement entropy

From the TTN approximation to the ground state of $H_{\text{Ising}}$ on a $L\times L$ torus for $L=\{4,6,8,10\}$ we can compute the entanglement entropy of one half and one quarter of the lattice at the critical point $\lambda=3.044$. Collecting results from Refs. 47–49, 55, and 56, at a quantum critical point, the entangle-

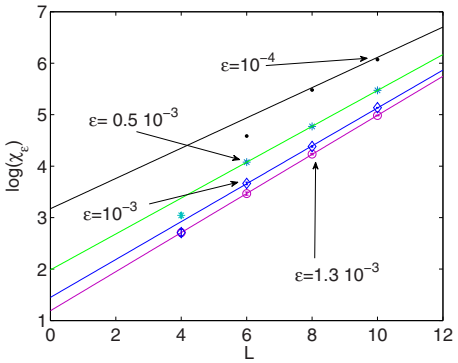


FIG. 26. (Color online) Plot of the logarithm of $\chi_\varepsilon$ as a function of $L$ for several choices of $\varepsilon$ in the range $10^{-4}\leq\varepsilon\leq 1.3\times 10^{-3}$. In each case, for $L$ large enough, the data lie on a straight line confirming that the cost of the simulation increases exponentially with the size $L$ of the system.

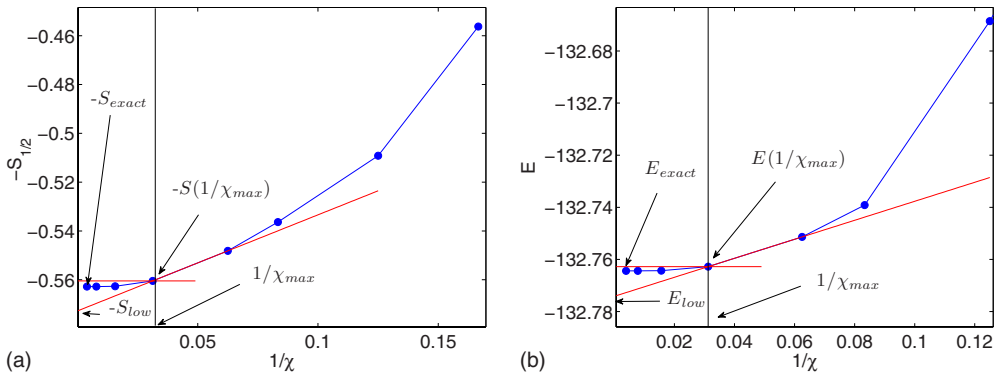


FIG. 27. (Color online) Analysis of $-S_{1/2}$ (top plot), minus the entanglement entropy of half a torus, for the critical Ising model on a $4\times4$ lattice, as a function of $1/\chi$ and the ground state energy (bottom plot). The exact result requires $\chi=256$. If we are only able to compute both observables for $\chi\leq32$ (the region in the plots on the right of the vertical black line) the values of both observables at $\chi=32$ provide an upper bound to their exact results. A lower bound is obtained by linearly extrapolating the two observables from the two best values at $\chi=16$ and $\chi=32$ to $1/\chi=0$. This is represented in the plots by the lower red line on the plots where the extrapolated values are denoted by $S_{low}$ and $E_{low}$. In this way it is clear that $-S_{low}\leq-S_{exact}\leq-S(1/\chi_{max})$ and $E_{low}\leq E_{exact}\leq E(1/\chi_{max})$ as expressed in Eq. (36) in the main text. The differences $|S(1/\chi_{max})-S_{low}|$ and $|E(1/\chi_{max})-E_{low}|$ thus provide upper bounds to the error for both $E$ and $S$ induced by considering a smaller $\chi$ than the one required by the exact solution.

ment entropy $S_{1/2}$ of half the torus, with total boundary $2L$, should scale as

$$S_{1/2}(L)=s_1 2L+\frac{s_{-1}}{2L}+\gamma_{QCP}, \tag{37}$$

where $\gamma_{QCP}$ (see Ref. 49, 51, and 54) should be a universal constant. We can now numerically confirm the validity of Eq. (37) and at the same time extract estimates for the coefficients in Eq. (37), including $\gamma_{QCP}$ for the Ising universality class on a torus. This is presented in Fig. 28 where, by performing a fit to the numerical data with Eq. (37), we obtain

$$s_1=0.067\ 01(107), \tag{38}$$

$$\gamma_{QCP}=0.030(26), \tag{39}$$

$$s_{-1}=-0.02(14), \tag{40}$$

with $\frac{\chi^2}{n.d.f.}=0.003$ (in this section of the work the letter $\chi^2$ refers to the standard name given to the sum of the residual in a least square fit, and should not be confuse with the truncation parameter of the TTN that is called $\chi$ through all the rest of work). The curve described by Eq. (37) is, hence, a good description of the scaling form of $S_{1/2}$. However the results we obtain are compatible with setting $s_{-1}$ to zero. If we do this, and repeat the fit we obtain

$$s_1=0.06722(18), \tag{41}$$

$$\gamma_{QCP}=0.0250(21), \tag{42}$$

with $\frac{\chi^2}{n.d.f.}=0.002$ (slightly lower than the previous case). The values for $s_1$ and $\gamma_{QCP}$ are also compatible with the ones of the previous fit. Their accuracy is however improved by one order of magnitude. These results suggest the absence of the correction term $s_{-1}$ in the scaling of the entanglement entropy of half a torus. It is interesting to notice that $\gamma_{QCP}$, that should be universal, is positive as predicted in Ref. 51.

Compiling results from Refs. 47–49, 55, and 56, the entropy $S_{1/4}$ of one quarter of the torus should scale as

$$S_{1/4}(L)=s_1 2L+\frac{s_{-1}}{2L}+s_0\log 2L+\text{const.} \tag{43}$$

where the presence of a logarithmic term is induced by the corners of the square block.[47,48,52,56] Comparing with Eq. (37) and using that the interacting boundary is the same for one half and one quarter of the torus, we can extract $s_0$ from

$$S_{1/4}(L)-S_{1/2}(L)=s_0\log 2L+\text{const.} \tag{44}$$

This study is presented in Fig. 29. The fit to the numerical data with Eq. (44) produces an estimate

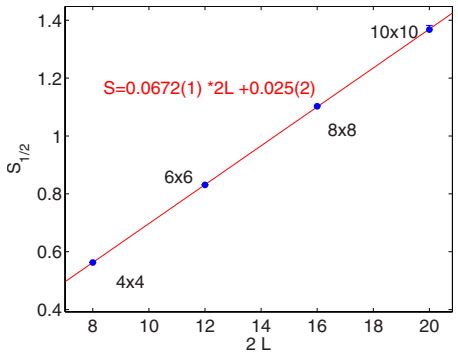


FIG. 28. (Color online) Entropy $S_{1/2}(L)$ of one half of the torus as a function of the linear size $L$, corresponding to the ground state of $H_{\text{Ising}}$ with $\lambda=3.044$. The results for $L=4$, 6, 8, and 10 confirm the linear growth predicted in Eq. (37), where no logarithmic correction is expected. The results of our study also seem to rule out the presence of the term proportional to $s_{-1}$. In the inset we show the results of the fit. The asymmetric errorbars, obtained through the analysis outlined in Sec. V D, are so small that they are hardly visible in the plot.

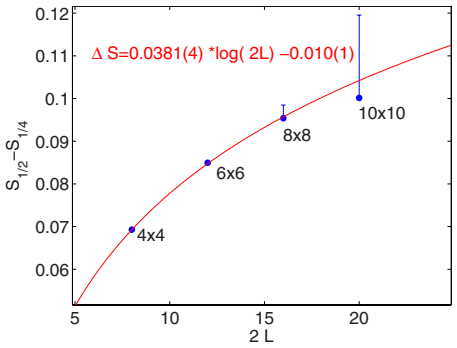


FIG. 29. (Color online) Difference between entropies for one quarter and one half of the torus as a function of the linear size $L$, corresponding to the ground state of $H_{\mathrm{Ising}}$ with $\lambda=3.044$. The results for $L=4$, 6, 8, and 10 allow us to confirm the logarithmic dependence predicted in Eq. (44), which is attributed to the presence of corners in the boundary of our block for one quarter of the lattice.

$$s_0 = -0.0381(4), \tag{45}$$

with a corresponding $\frac{\chi^2}{n.d.f.}=0.4$. This confirms the validity of the scaling form of Eq. (43) as well as a negative value for $s_0$ in agreement with the theory.[47,48,55,56]

As a side observation, this plot exemplifies once again the difference between the quasiexact and the approximate regime. The level of approximation we obtain for the $L=10$ system implies that those results are almost useless in extracting logarithmic corrections to the leading scaling laws.

### B. Renyi entropies

From the TTN approximation to the ground state, we can also compute all the Renyi entropies $S_n$

$$S_n = \frac{1}{1-n}\log \mathrm{tr}\,\rho^n \quad 0 \le n \le \infty \tag{46}$$

A limiting case of $S_n$ is given by the single copy entanglement $E^{(1)}$,[66]

$$E^{(1)} \equiv \lim_{n\to\infty} S_n. \tag{47}$$

$E^{(1)}$ is expected to have the same scaling form of Eq. (37) for the entanglement entropy but with different numerical coefficients,[50,54]

$$E^{(1)}_{1/2}(L) = e_1 2L + \frac{e_{-1}}{2L} + \gamma'_{QCP}. \tag{48}$$

The results for $E_1$ of half torus are shown in Fig. 30. The fit to the numerical data for $L=4$, 6, 8, and 10 with Eq. (48) produces

$$e_1 = 0.01724(20), \tag{49}$$

$$\gamma'_{QCP} = 0.0499(51), \tag{50}$$

$$e_{-1} = -0.161(30), \tag{51}$$

with $\frac{\chi^2}{n.d.f.}=0.0005$. This reveals a very good agreement between Eq. (48) and the numerical data. It is interesting to notice that the coefficient $e_{-1}$ is nonzero and negative, in agreement with the theory.[53] In addition, as already anticipated by the results contained in Ref. 50 and 54, the numerical values of the parameters for scaling of the single copy entanglement and entanglement entropy are different. Nevertheless, for the universal term, we find that

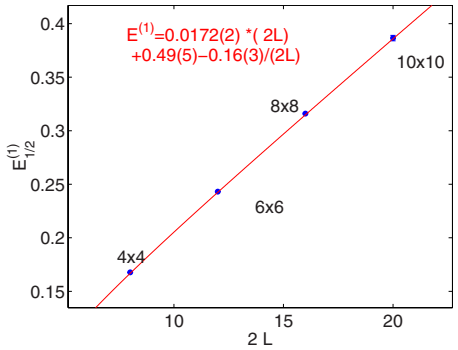


FIG. 30. (Color online) Single copy entanglement $E^{(1)}(L)$ for one half of the torus as a function of the linear size $L$, corresponding to the ground state of $H_{\mathrm{Ising}}$ with $\lambda=3.044$. The results for $L=4$, 6, 8, and 10 confirm the linear growth predicted in Eq. (48). In this case the term $e_{-1}$, analogous to the term $s_{-1}$ for the entanglement entropy, is negative as predicted by the theory. In the inset we present the results of the fit. The asymmetric error bars, obtained through the analysis outlined in Sec. V D, are so small that they are hardly visible on the plot.

$$\gamma'_{QCP} = 2\gamma_{QCP}, \tag{52}$$

to our numerical precision. This is reminiscent of a very similar result obtained for one dimensional critical chains, where the universal coefficient of the logarithmic scaling of the entanglement entropy with the size of the interval is two times [instead than one half as in Eq. (52)] the analogous coefficient for the scaling of the single copy entanglement.[67,68]

## VII. DISCUSSION

In this manuscript we have described a numerical technique based on a TTN to compute ground-state properties of 2D lattice systems. The approach exploits the entropic area law and has a cost that scales exponentially in the linear size of the lattice. Its goals are necessarily more modest than those of scalable tensor network algorithms such as PEPS and MERA.[4–14]

For the model we have considered here, the TTN approach offers a simple, effective way of obtaining quasiexact results well beyond what is possible with exact diagonalization techniques.[1,2] We expect that similar gains would also occur for other models. We envisage that this technique will become a useful tool both to study small lattice systems and in investigations based on finite-size scaling. A highlight of the approach is its simplicity, especially when compared to the scalable tensor network algorithms. In addition, it can be used to study block entropies, a task that becomes much less straightforward with other methods.

The TTN algorithm is closely related to the DMRG algorithm applied to 2D lattices. It is beyond the scope of the

present work to conduct the detailed analysis required to establish how the performances of the two algorithms compare. Nevertheless, some preliminary observations can be made. Updating the matrix product state (MPS) used in DMRG has a cost of $O(\chi^3 L^2)$ per sweep, while updating the TTN costs $O(\chi^4 L)$. This allows DMRG to consider values of $\chi$ that are about 10 times larger with similar computational cost. On the other hand the TTN has better connectivity. In a TTN all lattice sites are connected through the product of at most $O(\log L)$ tensors. Instead, when an MPS is used to encode the ground state of a 2D lattice, nearest-neighbor lattice sites are typically connected through the product of $O(L)$ tensors, with a fraction of the sites being connected through the product of $O(L^2)$ tensors (on a torus). As a result, we expect convergence to the ground state to be faster using a TTN. In addition, space symmetries can be (partially) incorporated in a TTN.

The TTN is particularly fitted to study entropies and their scaling with the size of the system. In this work we have reported some numerical results that are compatible with the expectation drawn from Refs. 47–49 and 55 about the presence, in the scaling form of the entanglement entropy, of both additive logarithmic and constant corrections to the area law. Our results suggest the absence of a $1/L$ correction. After the first draft of our paper was presented, a systematic study of all the Renyi entropies was reported in Ref. 54. This motivated us to also consider the single copy entanglement $E^{(1)}$, Eq. (47). We have confirmed that the scaling of $E^{(1)}$ also includes a constant additive correction to the area law and a term proportional to $1/L$, with numerical values different from the ones present in the scaling of the entanglement entropy. This is a hint to the presence of a different set of universal constants for each of the Renyi entropies as stated in Ref. 54. Further aspects of these scenarios can be found in Ref. 69.

## ACKNOWLEDGMENTS

The authors thank Philippe Corboz, Ian McCulloch, and Robert Pfeifer for useful conversations and technical advice. We also would like to thank F. Gliozzi, M. Huerta, and C. Hamer for useful correspondence. Financial support from the Australian Research Council (Grants No. APA FF0668731 and No. DP0878830) is acknowledged.

[1] C. J. Hamer, J. Phys. A **33**, 6683 (2000).
[2] M. Henkel, J. Phys. A **17**, L795 (1984).
[3] A. Laeuchli and C. Lhuillier, arXiv:0901.1065 (unpublished).
[4] F. Verstraete and J. I. Cirac, arXiv:cond-mat/0407066 (unpublished).
[5] V. Murg, F. Verstraete, and J. I. Cirac, Phys. Rev. A **75**, 033605 (2007).
[6] J. Jordan, R. Orus, G. Vidal, F. Verstraete, and J. I. Cirac, Phys. Rev. Lett. **101**, 250602 (2008).
[7] V. Murg, F. Verstraete, and J. I. Cirac, Phys. Rev. B **79**, 195119 (2009).
[8] G. Sierra and M. A. Martin-Delgado, arXiv:cond-mat/9811170 (unpublished).
[9] N. Maeshima, Y. Hieida, Y. Akutsu, T. Nishino, and K. Okunishi, Phys. Rev. E **64**, 016705 (2001).
[10] Y. Nishio, N. Maeshima, A. Gendiar, and T. Nishino, arXiv:cond-mat/0401115 (unpublished).
[11] Z. Gu, M. Levin, and X. Wen, Phys. Rev. B **78**, 205116 (2008).
[12] G. Vidal, Phys. Rev. Lett. **99**, 220405 (2007).
[13] G. Vidal, Phys. Rev. Lett. **101**, 110501 (2008).
[14] G. Evenbly and G. Vidal, Phys. Rev. Lett. **102**, 180406 (2009).
[15] G. Evenbly and G. Vidal, Phys. Rev. B **79**, 144108 (2009).
[16] M. Fannes, B. Nachtergaele, and R. F. Werner, J. Stat. Phys. **66**, 939 (1992).
[17] H. Niggemann, A. Klümper, and J. Zittartz, Z. Phys. B: Condens. Matter **104**, 103 (1997).
[18] B. Friedman, J. Phys.: Condens. Matter **9**, 9021 (1997).
[19] M. Lepetit, M. Cousy, and G. M. Pastor, Eur. Phys. J. B **13**, 421 (2000).
[20] M. A. Martin-Delgado, J. Rodriguez-Laguna, and G. Sierra, Phys. Rev. B **65**, 155116 (2002).
[21] Y. Shi, L. Duan, and G. Vidal, Phys. Rev. A **74**, 022320 (2006).
[22] D. Nagaj, E. Farhi, J. Goldstone, P. Shor, and I. Sylvester, Phys. Rev. B **77**, 214431 (2008).
[23] H. Otsuka, Phys. Rev. B **53**, 14004 (1996).
[24] L. P. Kadanoff, Physics **2**, 263 (1966).
[25] L. P. Kadanoff *et al.*, Rev. Mod. Phys. **39**, 395 (1967).
[26] K. G. Wilson, Rev. Mod. Phys. **47**, 773 (1975).
[27] M. E. Fisher, Rev. Mod. Phys. **70**, 653 (1998).
[28] T. W. Burkhardt and J. M. van Leeuwen, *Real-Space Renormalization* (Springer-Verlag, Berlin, 1982).
[29] L. P. Kadanoff, Phys. Rev. Lett. **34**, 1005 (1975).
[30] L. Bombelli, R. K. Koul, J. Lee, and R. D. Sorkin, Phys. Rev. D **34**, 373 (1986).
[31] M. Srednicki, Phys. Rev. Lett. **71**, 666 (1993).
[32] M. B. Plenio, J. Eisert, J. Dreissig, and M. Cramer, Phys. Rev. Lett. **94**, 060503 (2005).
[33] L. Masanes, arXiv:0907.4672 (unpublished).
[34] J. I. Latorre, E. Rico, and G. Vidal, Quantum Inf. Comput. **4**, 48 (2004).
[35] J. Eisert, M. Cramer, and M. B. Plenio, arXiv:0808.3773 (unpublished).
[36] S. R. White and R. M. Noack, Phys. Rev. Lett. **68**, 3487 (1992).
[37] S. R. White, Phys. Rev. Lett. **69**, 2863 (1992).
[38] R. M. Noack and S. R. White, Phys. Rev. B **47**, 9243 (1993).
[39] U. Schollwöck, Rev. Mod. Phys. **77**, 259 (2005).
[40] N. Shibata, J. Phys. A **36**, R381 (2003).
[41] S. R. White and A. L. Chernyshev, Phys. Rev. Lett. **99**, 127004 (2007).
[42] S. R. White and D. J. Scalapino, Phys. Rev. Lett. **80**, 1272 (1998).
[43] S. Liang and H. Pang, Phys. Rev. B **49**, 9214 (1994).
[44] P. Henelius, Phys. Rev. B **60**, 9561 (1999).
[45] M. S. L. du Croo de Jongh and J. M. J. van Leeuwen, Phys. Rev. B **57**, 8494 (1998).
[46] T. Xiang, J. Lou, and Z. Su, Phys. Rev. B **64**, 104414 (2001).

[47] H. Casini and M. Huerta, Nucl. Phys. B **764**, 183 (2007).
[48] E. Fradkin and J. E. Moore, Phys. Rev. Lett. **97**, 050404 (2006).
[49] B. Hsu, M. Mulligan, E. Fradkin, and E. Kim, Phys. Rev. B **79**, 115421 (2009).
[50] J. Stéphan, S. Furukawa, G. Misguich, and V. Pasquier, arXiv:0906.1153 (unpublished).
[51] E. Fradkin, arXiv:0906.1569 (unpublished).
[52] R. Yu, H. Saleur, and S. Haas, Phys. Rev. B **77**, 140402 (2008).
[53] H. Casini and M. Huerta, arXiv:0905.2562 (unpublished).
[54] M. A. Metlitski, C. A. Fuertes, and S. Sachdev, Phys. Rev. B **80**, 115122 (2009).
[55] H. Casini and M. Huerta, J. Stat. Mech. (2005) P12012.
[56] T. Nishioka, S. Ryu, and T. Takayanagi, arXiv:0905.0932 (unpublished).
[57] C. H. Bennett, H. J. Bernstein, S. Popescu, and B. Schumacher, Phys. Rev. A **53**, 2046 (1996).
[58] I. Affleck, T. Kennedy, E. H. Lieb, and H. Tasaki, Phys. Rev. Lett. **59**, 799 (1987).
[59] G. Vidal, Phys. Rev. Lett. **91**, 147902 (2003).
[60] S. Singh, R. N. C. Pfeifer, and G. Vidal, arXiv:0907.2994 (unpublished).
[61] I. P. McCulloch and M. Gulacsi, EPL **57**, 852 (2002).
[62] S. Singh, H. Q. Zhou, and G. Vidal, arXiv:cond-mat/0701427 (unpublished).
[63] H. Rieger and N. Kawashima, Eur. Phys. J. B **9**, 233 (1999).
[64] H. W. J. Blöte and Y. Deng, Phys. Rev. E **66**, 066110 (2002).
[65] M. P. Nightingale, Physica A **83**, 561 (1975).
[66] J. Eisert and M. Cramer, Phys. Rev. A **72**, 042112 (2005).
[67] R. Orus, J. I. Latorre, J. Eisert, and M. Cramer, Phys. Rev. A **73**, 060303(2006).
[68] I. Peschel and J. Zhao, J. Stat. Mech. (2005) P11002.
[69] F. Gliozzi and L. Tagliacozzo, arXiv:0910.3003 (unpublished).